Hints of natural supersymmetry in flavor anomalies?

P. S. Bhupal Dev[1,*] Amarjit Soni,[2,†] and Fang Xu[1,‡]

[1]*Department of Physics and McDonnell Center for the Space Sciences, Washington University,
St. Louis, Missouri 63130, USA*
[2]*Physics Department, Brookhaven National Laboratory, Upton, New York 11973, USA*

The recent results from the Fermilab muon $g - 2$ experiment, as well as the persisting hints of lepton flavor universality violation in B-meson decays, present a very strong case for flavor-nonuniversal new physics beyond the Standard Model. We assert that a minimal R-parity violating supersymmetric scenario with relatively light third-generation sfermions (dubbed as "RPV3") provides a natural, well-motivated framework for the simultaneous explanation of all flavor anomalies, while being consistent with a multitude of low-energy flavor constraints, as well as with limits from high-energy collider searches. We further propose complementary tests and distinct signatures of this scenario in the high-p_T searches at current and future colliders. Specifically, we find that an sbottom in the mass range of 2–12 TeV accounts for $R_{D^{(*)}}$ and $R_{K^{(*)}}$ flavor anomalies and it only plays a minor role in the $(g - 2)_\mu$ anomaly, whereas a sneutrino with mass between 0.7–1 TeV is the dominant player for $(g - 2)_\mu$. In this context, we propose specific collider signatures of sbottom via its decays to $\bar{t}(t)\mu^+\mu^-$, and of sneutrino pairs with their decays leading to a highly distinctive and spectacular four-muon final state, which can be used to completely probe the RPV3 parameter space of interest.

I. INTRODUCTION

This is an era of *anomalies*, as a growing list of experimental results, ranging from flavor physics to neutrinos to dark matter, show deviations from the Standard Model (SM) expectations at a few σ level [1]. While most of them might be an artifact (or a combination) of statistical fluctuations, systematic effects, theory/background uncertainties, experimental errors or other unknown issues that need further scrutiny, the intriguing possibility that some anomalies might represent genuine new physics signals makes it worthwhile studying all possible aspects, including beyond the SM (BSM) interpretations.

Of the existing statistically significant ($\gtrsim 3\sigma$) anomalies, particularly striking are the persistent hints of lepton flavor universality violation (LFUV) in semileptonic B-meson decays, as reported by three different experiments with completely independent datasets, namely, *BABAR* [2], Belle [3–7], and LHCb [8–12], with a combined

significance of 4.5σ [13]. Moreover, the LFUV observables expressed in term of the ratio of branching ratios (BRs) $R_{D^{(*)}}^{\tau/\ell} = \mathrm{BR}(B \to D^{(*)}\tau\bar{\nu})/\mathrm{BR}(B \to D^{(*)}\ell\bar{\nu})$ (with $\ell = e$, μ) and $R_{K^{(*)}}^{\mu/e} = \mathrm{BR}(B \to K^{(*)}\mu^+\mu^-)/\mathrm{BR}(B \to K^{(*)}e^+e^-)$, are theoretically clean, i.e. with strongly suppressed hadronic and Cabibbo-Kobayashi-Maskawa (CKM)-angle uncertainties, thus making them less vulnerable to higher-order quantum corrections [14,15]. There are also other intriguing aspects of data that deserve attention. For instance, as noticed in Ref. [16], there are 11 different measurements to date on the charged-current B-decays $B \to D^{(*)}\ell\nu$ and $B_c \to J/\psi\ell\nu$ (with $\ell = e$, μ, τ), *all* of which have experimental central values above the SM central value. Similarly, both R_K [12] and R_{K^*} [10] measurements from LHCb are consistently below the SM prediction of unity, which is a useful aspect of data that can be used to discriminate candidate BSM scenarios.[1] Also, the recently updated R_K measurement from LHCb with twice as much data [12] did not budge the central value from the old measurement (up to three decimal places, 0.846) [11]. With more statistics from LHCb and Belle-II expected in the near future, the status of the B anomalies should be further clarified.

*bdev@wustl.edu
†adlersoni@gmail.com
‡xufang@wustl.edu

---

[1]For example, some BSM scenarios with right-handed currents predict an anticorrelation between R_K and R_{K^*}.

Another long-standing anomaly that also hints at LFUV is the discrepancy between the SM and experimental values of the muon anomalous magnetic moment $(g-2)_\mu$ [17]. There has been an important recent development, as the first result from Fermilab $g-2$ experiment [18] is found to be compatible with the old BNL result [19] to six significant figures. When combined and compared with the world average of SM prediction [20], it increases the significance of the $(g-2)_\mu$ anomaly to 4.2σ [18]. This does require a very accurate theoretical prediction from the SM [20]. Over the years a systematically improvable strategy has been developed, based on a firm theoretical foundation of dispersion relations [21–23] and it has the power of being data driven (called the R-ratio method) [24–28]. In the meantime, a completely independent, nonperturbative, lattice simulation method, originally initiated in Ref. [29], has significantly matured over the years [30–36]; see Ref. [20] for a review. In fact, a new lattice result from the BMW Collaboration [36] already seems to have achieved competitive accuracy and claims compatibility between its SM calculation and the experimental result at 1.5σ. However, this result using a particular fermion-discretization method (staggered fermions) disagrees with the R-ratio results at $\approx 3.7\sigma$ [36,37] and is also in $\approx 2.5\sigma$ tension [37] with another lattice/data (window method) result of RBC-UKQCD Collaboration [31] using domain-wall fermions [38–41]. The domain-wall method essentially preserves the chiral symmetry of the continuum theory at any lattice spacing and therefore, domain wall fermions behave as continuumlike fermions so the corresponding chiral perturbation theory is very much continuumlike [42]. This is unlike the case of staggered fermions which involves many unphysical degrees of freedom that only decouple in the continuum limit, thus requiring a fairly cumbersome treatment of staggered chiral perturbation theory [43–45] for extrapolation to the continuum limit. For these reasons and many more,[2] widespread and long-standing understanding in the lattice community is that important physics results should be taken seriously *only after* there is consistency and agreement amongst results obtained in the continuum limit after use of as many different fermion discretization methods as possible.

Taken at face value, all three flavor anomalies, viz. $R_{D^{(*)}}$, $R_{K^{(*)}}$, and $(g-2)_\mu$, provide a strong evidence for some flavor-nonuniversal BSM physics, with a combined significance of more than 5σ [16]. With updates from Belle-II, LHCb and Fermilab expected soon, the chances are high that at least one of these anomalies will survive the test of time. Under such a watershed departure from the past, it is very likely that nature is also trying to address some long-standing, persistent issue(s) with the SM. One such basic concern with the SM is the fact that it is exceedingly fine tuned, *i.e. unnatural* due to radiative instability of the Higgs which primarily originates from the heaviness of the top quark, a member of the third generation. The LFUV observable $R_{D^{(*)}}$ involves $b \to c\tau\nu$, where at least two fermions are from the third generation. Taking this cue from experiment and keeping radiative stability issue in mind, along with minimality, we were originally led [50] to propose a minimal R-parity violating (RPV) super-symmetry (SUSY) framework with the third-generation superpartners lighter than the first two (hence dubbed as "RPV3") as a compelling BSM candidate for the $R_{D^{(*)}}$ anomaly. In a follow-up work [16], we presented a benchmark point where $R_{K^{(*)}}$ and $(g-2)_\mu$ can also be explained together with $R_{D^{(*)}}$ within the RPV3 framework. In this paper, we perform a comprehensive study of the minimal RPV3 parameter space that could simultaneously address all three flavor anomalies, in light of the recent updates and taking into account all relevant collider and flavor constraints. Let us assert that indeed there is a plethora of existing experimental constraints from Z, W, τ, D^0, B, B_s, and B_c decays, as well as $B_s - \bar{B}_s$ mixing, that have to be enforced on RPV3, thus making it rather restrictive. We then propose specific collider signatures, partly based on general crossing symmetry arguments, that could independently probe the preferred RPV3 region at the energy frontier. Such complementarity with the intensity frontier observables makes the RPV3 framework particularly predictive and testable in the near future.[3] While the RPV3 framework has many nice features, it does possess two appreciable caveats which we will briefly discuss towards the end.

The rest of the paper is organized as follows: In Sec. II, we review the RPV3 framework and present all relevant expressions for the RPV3 explanation of the flavor anomalies. In Sec. III, we present a numerical scan of a 6-dimensional RPV3 parameter space. In Sec. IV, we choose three benchmark points from our numerical scan and illustrate the allowed regions preferred by the anomalies. In Sec. V, we propose some collider signals that can be used an independent test of the anomalies. In Sec. VI, we discuss possible ways to distinguish the RPV3 model from other BSM scenarios. Our conclusions are given in Sec. VII. In the Appendix, we give some details of the low-energy constraints used in our analysis.

---

[2]For instance, another concern raised with the BMW result is that if a change in the hadronic vacuum polarization contribution brings the SM value of $(g-2)_\mu$ closer to the experimental value as claimed by the BMW Collaboration, it might lead to other problems in global electroweak fit [46–49] (see also the rebuttal in Ref. [36]).

[3]Note also that there is significant motivation and rationale for this theoretical scenario from an entirely different perspective [51]. Moreover, due to renormalization group evolution effects, heavy first two generations play a significant role in obtaining the observed 125 GeV Higgs mass, which makes this model less fine tuned than the constrained minimal supersymmetric SM (cMSSM) [52,53].

II. RPV3 FRAMEWORK

The effective number of degrees of freedom relevant to the three LFUV observables in RPV3 is of $\mathcal{O}(36)$ whereas in the SM it is of $\mathcal{O}(15)$. So the question might arise: What have we gained at the expense of doubling the degrees of freedom? The answer is that it has a deeper Bose-Fermi symmetry rationale, and many associated attractive features of SUSY automatically in-built, such as radiative stability of the Higgs boson, radiative neutrino masses, radiative electroweak symmetry breaking, stability of the electroweak vacuum, gauge coupling unification, (gravitino) dark matter and baryogenesis [54]. Moreover, as a necessary generalization of the Yang-Mills theory [55], all the interactions allowed by the enlarged internal symmetry of the theory must be included, which readily removes the accidental flavor symmetry of the SM and leads naturally to LFUV. Our RPV3 framework also has other nontrivial features that are consistent with the experimental observations, such as having both R_K and R_{K^*} less than one and the D^* and tau polarizations essentially the same as in the SM, both of which come automatically because RPV3 subsumes the chiral gauge couplings of the SM.

It is worth noting here that the semileptonic B-meson decays in question involve interactions of a bottom quark, a member of the third generation, in terms of either $b \to c\ell^-\bar{\nu}$ or $b \to s\ell^+\ell^-$ transitions. Analogous semileptonic decays of charmed mesons $D \to X\ell^+\nu$ ($X = \pi$, K, ω, η, ρ) [56–60], all involving $c \to d\ell^+\nu$ transition, as well as the ratio of the rates of leptonic kaon decays $K^\pm \to e^\pm\nu$ and $K^\pm \to \mu^\pm\nu$ [61,62], and of Λ-baryon decays $\Lambda \to pe^-\bar{\nu}$ and $\Lambda \to p\mu^-\bar{\nu}$ [63] are all in complete agreement with the SM. Therefore, it is conceivable that the third-generation fermions are special in the SM, and in the same vein, we take the third-generation sfermions to be special in RPV3 (similar to the "natural SUSY" hypothesis [51,64]).

The $R_{D^{(*)}}$ anomaly can be accommodated in RPV3 at tree level via the LQD interactions [50,65–71],

$$\mathcal{L}_{LQD} = \lambda'_{ijk}[\tilde{\nu}_{iL}\bar{d}_{kR}d_{jL} + \tilde{d}_{jL}\bar{d}_{kR}\nu_{iL} + \tilde{d}^*_{kR}\bar{\nu}^c_{iL}d_{jL}$$
$$- \tilde{e}_{iL}\bar{d}_{kR}u_{jL} - \tilde{u}_{jL}\bar{d}_{kR}e_{iL} - \tilde{d}^*_{kR}\bar{e}^c_{iL}u_{jL}] + \text{H.c.}. \quad (1)$$

Similarly, the $R_{K^{(*)}}$ anomaly can be explained via both tree and loop-level LQD interactions alone or together with LLE interactions [67,68,70,72–76],

$$\mathcal{L}_{LLE} = \frac{1}{2}\lambda_{ijk}[\tilde{\nu}_{iL}\bar{e}_{kR}e_{jL} + \tilde{e}_{jL}\bar{e}_{kR}\nu_{iL} + \tilde{e}^*_{kR}\bar{\nu}^c_{iL}e_{jL}$$
$$- (i \leftrightarrow j)] + \text{H.c.}. \quad (2)$$

The muon $g - 2$ gets additional contributions from both LQD and LLE terms [77], but as we will see later, the LLE
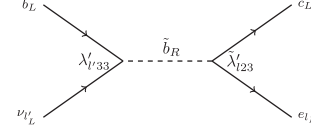

FIG. 1. RPV3 contribution to $R_{D^{(*)}}$ via sbottom exchange involving λ' couplings. Here $\tilde{\lambda}'_{ijk}$ is defined as $\lambda'_{ilk}V_{jl}$ (with V_{jl} being the CKM matrix elements). The complete set of diagrams can be found in Ref. [16].

contribution is more relevant for our parameter space of interest.[4]

Out of the $3^3 = 27$ independent RPV couplings λ'_{ijk} in Eq. (1) and the $3^2 = 9$ independent λ_{ijk} (since it is antisymmetric in the first two indices, i.e. $\lambda_{ijk} = -\lambda_{jik}$) in Eq. (2), we only consider those involving third-generation sfermions in our RPV3 framework. In what follows, we calculate the RPV3 contributions to the flavor anomalies.

A. R_D and $R_{D^{(*)}}$

The $b \to c\ell\nu$ transition relevant for the $R_{D^{(*)}}$ anomaly gets a BSM contribution at tree level from the LQD interactions via the right-handed sbottom ($\tilde{b}_R$) exchange, as shown in Fig. 1. It gives rise to a SM-like effective Hamiltonian

$$\mathcal{H}^{b \to c\ell\nu}_{\text{eff}} = \frac{4G_F}{\sqrt{2}}V_{cb}(1 + C_{V_L})\mathcal{O}_{V_L} + \text{H.c.}, \quad (3)$$

[where G_F is the Fermi constant and V_{cb} is the (2,3) CKM element] with the operator $\mathcal{O}_{V_L} = (\bar{c}_L\gamma^\mu b_L)(\bar{\ell}_L\gamma_\mu\nu_{\ell L})$ with a corresponding coefficient $C_{V_L} \simeq 0.09$, as preferred by the q^2 and D^* polarization data [80]. We then have [68]

$$\frac{R_D}{R_D^{\text{SM}}} = \frac{R_{D^*}}{R_{D^*}^{\text{SM}}} = \frac{|\Delta^c_{31}|^2 + |\Delta^c_{32}|^2 + |1 + \Delta^c_{33}|^2}{|\Delta^c_{21}|^2 + |1 + \Delta^c_{22}|^2 + |\Delta^c_{23}|^2},$$

$$\text{with} \quad \Delta^c_{ll'} = \frac{v^2}{4m^2_{\tilde{b}_R}}\lambda'_{l'33}\left(\lambda'_{l33} + \lambda'_{l23}\frac{V_{cs}}{V_{cb}} + \lambda'_{l13}\frac{V_{cd}}{V_{cb}}\right), \quad (4)$$

$v = (\sqrt{2}G_F)^{-1/2}$ being the electroweak scale. The $R_{D^{(*)}}$ anomaly can be explained for the ratio in Eq. (4) being 1.15 ± 0.04 [16], which dictates the $R_{D^{(*)}}$-allowed parameter space in the $(m_{\tilde{b}_R}, \lambda'_{lk3})$ plane.

From Eq. (1) we see that for the LQD interactions in RPV3, the dimension-six effective interaction for the semileptonic $B \to D^{(*)}$ decays is essentially identical to the $(V - A) \times (V - A)$ structure of the SM effective

---

[4]The simultaneous presence of λ and λ' couplings is consistent with proton decay constraints, as long as the relevant λ'' (UDD-type) couplings are sufficiently suppressed [54], which can be done using a baryon triality [78,79].

Hamiltonian (after the appropriate Fierz transformation) with the difference being just in the overall coefficient. Therefore, the fact that the experimentally observed q^2 distribution and the D^* and τ polarizations prefer the $\mathcal{O}_{V_L}$ operator [80] is consistent with our RPV3 scenario.

In presence of LLE interactions, there is another contribution to $R_{D^{(*)}}$ from RPV3 with left-handed stau exchange [16]; however, this involves right-handed bottom and charged lepton, and the corresponding effective operator $\mathcal{O}_{V_R}$ does not provide the best fit to the $b \to c\ell\nu$ observables [80]. Therefore, we choose the coupling $\lambda'_{323} = 0$ so that the stau channel is not relevant. Similarly, for a light neutralino $\tilde{\chi}$, there are additional contributions involving $B \to D^{(*)}\ell\tilde{\chi}$, which however turn out to be subdominant [16].

It is also important to note that in the MSSM with two Higgs doublets, there is a standard R-parity conserving (RPC) contribution to $b \to c\ell\nu$ due to charged Higgs exchange. But this goes in the wrong direction and is much smaller for R_{D^*} [81,82]. Moreover, this is in tension with LHC mono-τ data [83] and also induces a large BR$(B_c \to \tau\nu) > 50\%$ which is problematic [84–86] (see however Ref. [87]). Therefore, one must resort to the RPV interactions given above to explain the $b \to c\ell\nu$ anomalies within a SUSY framework.

B. R_K and $R_{K^{(*)}}$

As for the $R_{K^{(*)}}$ anomaly involving $b \to s\ell^+\ell^-$ transitions, simultaneous RPV contributions to electron and muon final states would be strongly constrained by lepton flavor violating (LFV) searches like $\mu \to e\gamma$. Therefore, we only consider corrections to the muonic channel, as preferred by recent global fits [88]. The relevant effective Hamiltonian is

$$\mathcal{H}_{\text{eff}}^{b \to s\ell\ell} = -\frac{4G_F}{\sqrt{2}} V_{ts}^* V_{tb} \frac{e^2}{16\pi^2} \sum_{i=9,10} [C_i^\ell Q_i^\ell + C_i'^\ell Q_i'^\ell], \quad (5)$$

with the operators $Q_9^\ell = (\bar{s}\gamma_\alpha P_L b)(\bar{\ell}\gamma^\alpha \ell)$, $Q_{10}^\ell = (\bar{s}\gamma_\alpha P_L b)(\bar{\ell}\gamma^\alpha \gamma_5 \ell)$, and $Q'_{9,10}$ are obtained from $Q_{9,10}$ by replacing $P_L \to P_R$. Global fits of all relevant data, including the angular observables or absolute rate for $B \to K^{(*)}\mu^+\mu^-$ and also the rate for $B_s \to \phi\mu^+\mu^-$, prefer the Wilson coefficients $C_9^\mu = -C_{10}^\mu = -0.35 \pm 0.08$ [88], whereas $C_9'^\mu$ and $C_{10}'^\mu$ are compatible with zero at 2σ level.

In the RPV3 scenario, new contributions to $b \to s\ell\ell$ transitions arise both at tree and loop levels. Tree-level exchange of stops gives contributions to the wrong chirality Wilson coefficients [73], which can be translated into an approximate 3σ confidence level (CL) upper bound on

$$|\lambda'_{233}\lambda'_{232}| \lesssim 10^{-3} \times \left(\frac{m_{\tilde{\tau}_L}}{1 \text{ TeV}}\right)^2. \quad (6)$$
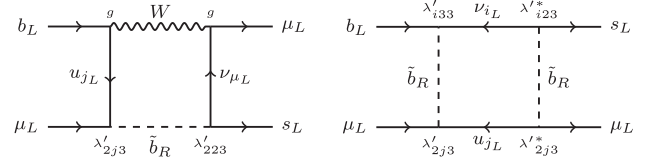

FIG. 2. Representative box diagrams for the dominant RPV3 contributions to $b \to s\mu^+\mu^-$ in our scenario. The complete set of diagrams can be found in Ref. [16].

This can be satisfied by either making the stop relatively heavier, or by setting one of λ'_{23k} (with $k = 2$ or 3) small.

At the one-loop level, there are new contributions to $b \to s\ell\ell$ with sbottoms, stops, staus, and sneutrinos in the loop [16,68,73,74]. For the minimal RPV3 case considered here, the only relevant diagrams are those shown in Fig. 2 and the resulting Wilson coefficients (after taking into account all possible combinations of box diagrams) are given by

$$C_9^\mu = -C_{10}^\mu = \frac{m_t^2}{m_{\tilde{b}_R}^2} \frac{|\lambda'_{233}|^2}{16\pi\alpha_{\text{em}}} - \frac{v^2}{m_{\tilde{b}_R}^2} \frac{X_{bs}X_{\mu\mu}}{64\pi\alpha_{\text{em}} V_{tb}V_{ts}^*}, \quad (7)$$

where $X_{bs} = \sum_{i=1}^3 \lambda'_{i33}\lambda'_{i23}$ and $X_{\mu\mu} = \sum_{j=1}^3 |\lambda'_{2j3}|^2$. Requiring Eq. (7) to match the global-fit result yields the $R_{K^{(*)}}$-allowed parameter space in the $(m_{\tilde{b}_R}, \lambda'_{lk3})$ plane. Note that the correlation between R_K and $R_{K^{(*)}}$, i.e. both going in the same direction is automatically obtained in the RPV3 setup because of the same underlying gauge structure as in the SM.

It is important to note here that in the MSSM with RPC couplings only, the only way to get lepton-flavor nonuniversal contribution to $b \to s\ell\ell$ is through box diagrams with light winos (or binos) and large nonuniversality in slepton masses [89,90]. However, in order to get the required $C_9^\mu \sim -0.35$, one needs an extremely light spectrum of winos and smuons around 100 GeV and sbottoms around 500 GeV, which are ruled out by the LHC data [91]. Therefore, just like in the case of $R_{D^{(*)}}$, the explanation of the $R_{K^{(*)}}$ anomaly within SUSY requires one to invoke RPV interactions.

C. $(g-2)_\mu$

The RPV3 contributions to $(g-2)_\mu$ can arise from both λ and λ' couplings [77], as shown in Fig. 3,

$$\Delta a_\mu = \frac{m_\mu^2}{96\pi^2} \sum_{k=1}^3 \left(\frac{2(|\lambda_{32k}|^2 + |\lambda_{3k2}|^2)}{m_{\tilde{\nu}_\tau}^2} - \frac{|\lambda_{3k2}|^2}{m_{\tilde{\tau}_L}^2} - \frac{|\lambda_{k23}|^2}{m_{\tilde{\tau}_R}^2} + \frac{3|\lambda'_{2k3}|^2}{m_{\tilde{b}_R}^2} \right), \quad (8)$$

which should be compared with the observed discrepancy of $\Delta a_\mu^{\text{obs}} = (251 \pm 59) \times 10^{-11}$ [18]. Note that the stau
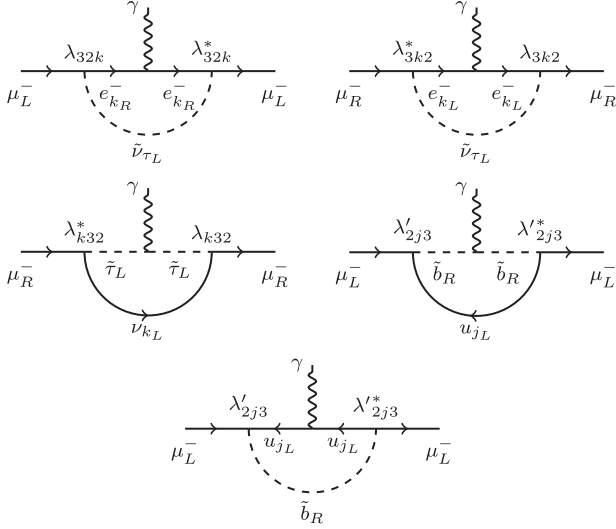
FIG. 3. Relevant contribution to the $(g-2)_\mu$ from λ and λ' couplings in our RPV3 scenario. The complete set of diagrams can be found in Ref. [16].

contributions are of the wrong sign, and therefore, are required to be subdominant by making the staus relatively heavier. As we will see later, the λ contribution to $(g-2)_\mu$ from sneutrinos is dominant over the λ' contribution from sbottoms in our RPV3 scenario. There are other diagrams, as shown in Ref. [16], which are not relevant to our discussion. For instance, the stop-mediated diagrams cancel, so are not shown in Fig. 3. Similarly, the diagram with right-handed stau mediator does not contribute because one of the corresponding couplings is assumed to be zero here.

There are additional RPC SUSY contributions to Δa_μ involving smuons and muon sneutrinos [92–94]. However, since these second-generation sfermions are decoupled from the low-energy theory in RPV3, we only focus on the RPV contributions.

III. NUMERICAL SCAN

Our aim is to find the *minimum* set of RPV3 model parameters that could simultaneously address all three flavor anomalies, while being consistent with all other low-energy flavor constraints (for a detailed discussion and explicit expressions, see the Appendix and Ref. [16])[5] and the high-energy LHC data, while at the same time giving rise to potentially observable collider signals as an independent test of the anomalies. To this effect, we choose to work with the following 6-dimensional parameter space that turns out to be the most important for pursuing collider implications,

$$\{\lambda_{232}, \lambda'_{233}, \lambda'_{223}, \lambda'_{232}, m_{\tilde{b}_R}, m_{\tilde{\nu}_\tau}\} \qquad (9)$$

and drop the other couplings and masses from our discussion (unless otherwise specified).[6] As for the above choice of our couplings, note that once we choose a nonzero $\lambda_{232} = -\lambda_{322}$ to explain the $(g-2)_\mu$ anomaly [c.f. Eq. (8)], other relevant λ_{3ij} couplings cannot be large at the same time due to the constraints from LFV decays $\tau^- \to \mu^+\mu^-\mu^-$ and $\mu \to e\gamma$. Similarly, only some of the λ'_{2ij}'s are allowed to be large at the same time as λ_{232}; if instead we chose λ'_{3ij}, for instance, combined with λ_{232} and light tau-sneutrino propagator, this will lead to strong tree-level meson decays $\bar{d}_i d_j \to \mu^+\mu^-$. Note that due to our choice of couplings (i.e. $\lambda'_{3ij} = 0$), we do not have the single production of tau-sneutrino at the LHC, and therefore, only discuss their pair production in the main text.

As for omitting the remaining third-generation sfermion masses from Eq. (9), the right-stau mass $m_{\tilde{\tau}_R}$ is irrelevant, because it only enters in the $(g-2)_\mu$ expression (8), but with the coupling λ_{k23}, which is set to zero for our benchmark points. The left-stau term in Eq. (8) has a negative contribution and its effect can be ignored for $m_{\tilde{\tau}_L} \gtrsim \mathcal{O}(2\,\text{TeV})$. For concreteness, we will just set $m_{\tilde{\tau}_L} = 4$ TeV in the following analysis. Similarly, the left-stop mass $m_{\tilde{t}_L}$ only influences the C_9' and C_{10}' [cf. Eq. (6)] and the $B_s \to \mu^+\mu^-$ constraint, if both λ'_{233} and λ'_{232} are large at the same time. When this is the case, we can make $m_{\tilde{t}_L}$ appropriately heavier using Eq. (6) without affecting any other observable; therefore, we do not include $m_{\tilde{t}_L}$ in Eq. (9). Finally, the left-sbottom mass $m_{\tilde{b}_L}$ does not influence the anomaly observables, but is only relevant for constraints like $b \to s\gamma$, $B \to K\nu\bar{\nu}$ and B_s-$\bar{B}_s$; so wherever applicable, we will just set $m_{\tilde{b}_L} = m_{\tilde{b}_R}$ for simplicity.

We then perform a random scan over the 6-dimensional parameter space given in Eq. (9) with the following ranges:

$$|\lambda_{232}| \in [2.5, 3.5], \qquad |\lambda'_{233}| \in [0.01, 3],$$
$$|\lambda'_{223}| \in [0.01, 3], \qquad |\lambda'_{232}| \in [0.01, 3],$$
$$m_{\tilde{b}_R} \in [1.2, 10]\,\text{TeV}, \qquad m_{\tilde{\nu}_\tau} \in [0.7, 1.2]\,\text{TeV}, \quad (10)$$

and look for solutions that could simultaneously explain $R_{D^{(*)}}$, $R_{K^{(*)}}$ and $(g-2)_\mu$ anomalies at either 2σ or 3σ, while being consistent with all the low-energy constraints discussed above. Out of 30 million points scanned, we only found 1570 solutions, as shown by the scatter plots in Fig. 4. Note that the lower edges of the $m_{\tilde{\nu}_\tau}$ and $m_{\tilde{b}_R}$ scan ranges correspond to the current LHC limits (see Sec. V).
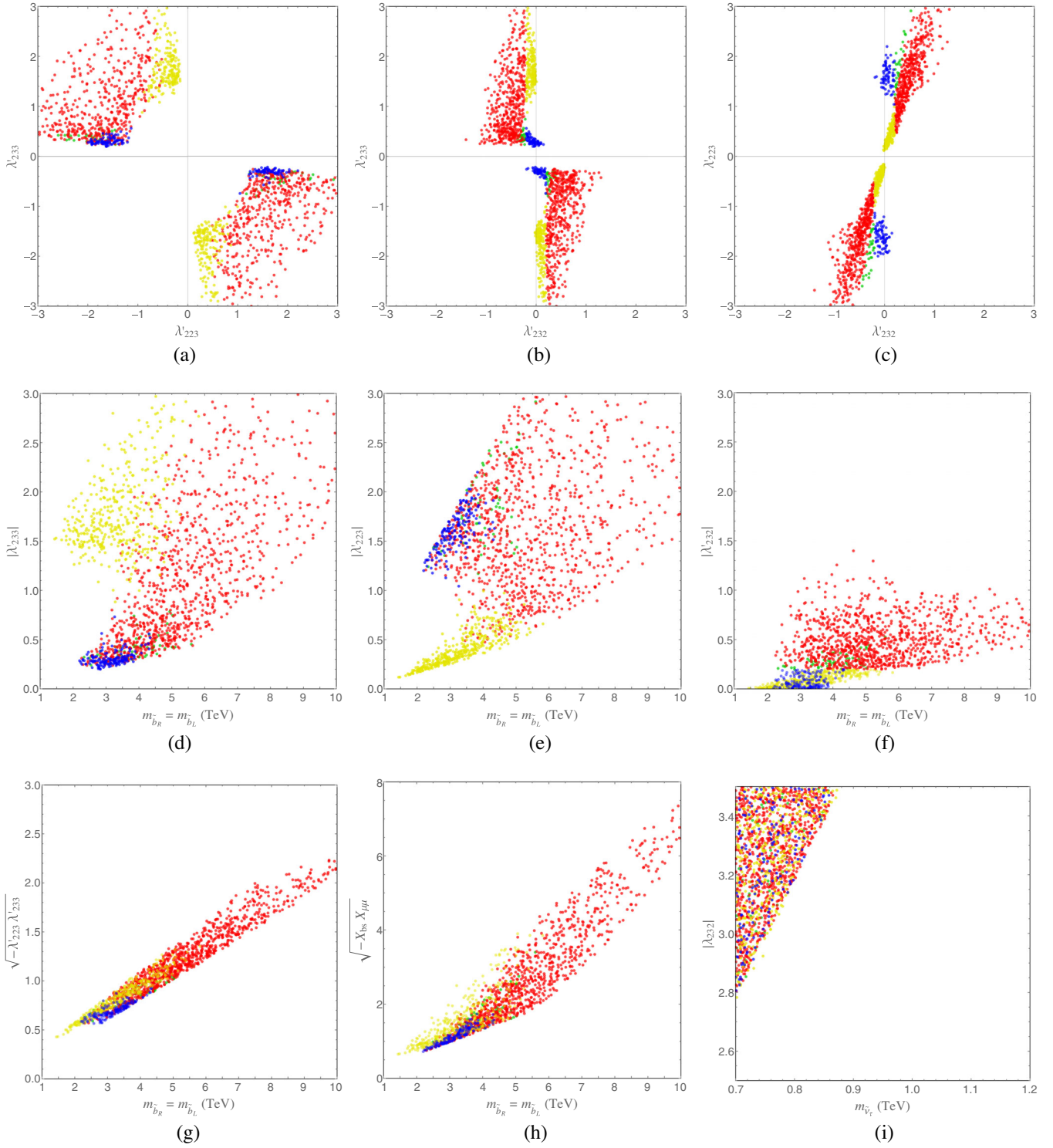
FIG. 4.   Scatter plots showing the correlations between various RPV3 parameters in Eq. (9). All these points can simultaneously explain $R_{D^{(*)}}$, $R_{K^{(*)}}$, and $(g-2)_\mu$ anomalies at 3σ CL, while being consistent with all the low-energy and LHC constraints. The yellow (blue) points correspond to $|\lambda'_{232}| < 0.2$ and $|\lambda'_{223}| < (>)1$. The red points correspond to $|\lambda'_{232}| > 0.2$ and $1.5 < \lambda'_{223}/\lambda'_{232} < 5.5$. The green points correspond to the crossover region from red to blue. The three benchmark points (BP1, BP2, BP3) discussed in the text are taken respectively from the densest regions of the red, yellow. and blue solutions.

We divide all the obtained solutions into three characteristically different regions, as shown by the red, blue and yellow points in Fig. 4. In particular, from Fig. 4(c), we see that the yellow (blue) points correspond to $|\lambda'_{232}| < 0.2$ and $|\lambda'_{223}| < (>)1$, while the red points correspond to $|\lambda'_{232}| > 0.2$ and $1.5 < \lambda'_{223}/\lambda'_{232} < 5.5$, and the green points simply correspond to the crossover region from red to blue. We can immediately make several observations from these plots, as follows:

(i) From Figs. 4(b) and 4(c), we see that there are both yellow and blue solutions with very small (or almost vanishing) λ'_{232} which means that for these points, we can automatically satisfy the $C'_9 - C'_{10}$ constraint discussed in main text, as well as the $B_s \to \mu^+\mu^-$ constraint for any value of the stop mass.

(ii) From Fig. 4(c), we see that the red points cluster around $\lambda'_{223}/\lambda'_{232} \sim 3$; this helps to avoid the $B_s - \bar{B}_s$ constraint due to an accidental cancellation.

(iii) From Figs. 4(a)–(c), we find that λ'_{233} and λ'_{223} must have opposite signs. This is mainly needed to make the second term of Eq. (7) negative in order to satisfy the $R_{K^{(*)}}$ anomaly. Similarly, λ'_{223} and λ'_{232} are preferred to have the same sign to get cancellation in $B_s - \bar{B}_s$ mixing. On the other hand, as Eq. (8) suggests and as shown in Fig. 4(i), the sign of λ_{232} does not matter.

(iv) According to Fig. 4(i), the different colored points are totally mixed, which implies mutual orthogonality between the $(m_{\tilde{\nu}_\tau}, \lambda)$ and $(m_{\tilde{b}_R}, \lambda')$ parameter spaces. In other words, $(m_{\tilde{\nu}_\tau}, \lambda)$ mostly influences the $(g-2)_\mu$ solutions, whereas $(m_{\tilde{b}_R}, \lambda')$ influences the $R_{D^{(*)}}$ and $R_{K^{(*)}}$ solutions and the low-energy flavor constraints. This is further illustrated in Figs. 5 and 6.

(v) From Fig. 4(e), we find that $|\lambda'_{223}| \lesssim 0.57$ $(m_{\tilde{b}_R}/1 \text{ TeV})$, which is mainly due to the $D^0 \to \mu^+\mu^-$ constraint. Similarly, from Fig. 4(d), we get $|\lambda'_{233}| \lesssim 1.0$ $(m_{\tilde{b}_R}/1 \text{ TeV})$. These two conditions imply that the λ' contributions to $(g-2)_\mu$ in Eq. (8) cannot be large; therefore, the bulk of the RPV3 contribution must come from the λ sector, which requires relatively larger $\lambda_{232} \gtrsim 2.8$ and smaller $m_{\tilde{\nu}_\tau} \lesssim 0.9$ TeV (to keep λ_{232} perturbative) to satisfy the $(g-2)_\mu$ anomaly, as confirmed in Fig. 4(i).

(vi) From Fig. 4(g), we find that $\sqrt{-\lambda'_{223}\lambda'_{233}} \sim (0.20 - 0.28)$ $(m_{\tilde{b}_R}/1 \text{ TeV})$, which mainly comes from the $B \to K\nu\bar{\nu}$ constraint.

(vii) From Fig. 4(a), we find that for the yellow and blue points, $|\lambda'_{233}\lambda'_{223}|$ is small to satisfy the $B_s - \bar{B}_s$ mixing constraint.

(viii) From Fig. 4(f), we see that $|\lambda'_{232}| \lesssim 1.5$. Thus, according to Fig. 4(c), $|\lambda'_{232}|$ should be either small (yellow and blue) or $\sim|\lambda'_{223}|/3$ (red). Also, from

Fig. 4(d), $|\lambda'_{233}| \gtrsim 0.20$ and from Fig. 4(e), $|\lambda'_{223}| \gtrsim 0.12$.

(ix) Figs. 4(d)–4(f) suggest that $m_{\tilde{b}_R} \gtrsim 1.44$ TeV, slightly stronger than the direct LHC bound of 1.23 TeV [96].

(x) Fig. 4(h) gives the range of $X_{bs}X_{\mu\mu}$ for the RPV3 contribution to $R_{K^{(*)}}$, since the second term in Eq. (7) gives the correct sign, whereas the first term gives the wrong sign.

IV. BENCHMARK POINTS

We will choose our benchmark points for the collider study in the next section based on the results of our numerical scan in Fig. 4 and the above mentioned observations. Specifically, we choose three benchmark points (BP1, BP2, and BP3), one each from the red (BP1), yellow (BP2), and blue (BP3) solutions found above.

(a) *BP1 (Red):* $\lambda'_{233} = -\lambda'_{223} = -3\lambda'_{232}$. The allowed region in this case is shown in Fig. 5(a) by the red shaded region.

(b) *BP2 (Yellow):* $\lambda'_{233} = -8\lambda'_{223}$, $\lambda'_{232} = 0$. The allowed region in this case is shown in Fig. 5(b) by the yellow shaded region.

(c) *BP3 (Blue):* $\lambda'_{223} = -6\lambda'_{233}$, $\lambda'_{232} = 0$. The allowed region in this case is shown in Fig. 5(c) by the blue shaded region.

The size of the allowed region in each case is directly correlated with the density of the corresponding points in Fig. 4. Therefore, our BP1 is taken from the densest region of the red solution, in order to maximize the overlap region in Fig. 5. For BP2 and BP3, we just choose $\lambda'_{232} = 0$ for simplicity. Since the λ coupling and the tau-sneutrino mass are relevant only for $(g-2)_\mu$, we fix $\lambda_{232} = -\lambda_{322} = 2.8$ and $m_{\tilde{\nu}_\tau} = 0.7$ TeV (see Fig. 6) in all three cases to explain the $(g-2)_\mu$ anomaly at 3σ (2σ) CL, as shown by the orange shaded regions with solid (dashed) boundaries in Fig. 5.

In BP1, since both λ'_{233} and λ'_{232} are nonzero, there is a lower limit on the stop mass from the $C'_9 - C'_{10}$ constraint [cf. Eq. (6)]; $m_{\tilde{t}_L} \gtrsim (14-40)$ TeV for the overlap region.[7] However, this limit does not apply for BP2 and BP3, since $\lambda'_{232} = 0$ in those cases; therefore, the stop can be as light as the current LHC bound of ~ 800 GeV [91] in these cases. We have also checked that the constraints from $B_s \to \mu^+\mu^-$, whose amplitude is proportional to $C^\mu_{10} - C'^\mu_{10}$ [99], is easily satisfied for all three BPs, with the RPV3 contribution to $\text{BR}(B_s \to \mu^+\mu^-) \lesssim 10^{-12}$, well below the current experimental precision; $\text{BR}(B_s \to \mu^+\mu^-)_{\text{exp}} = (2.69^{+0.37}_{-0.35}) \times 10^{-9}$ [100].

---

[7]According to Ref. [98], stop masses lower than about 10 TeV are preferred from naturalness point of view. For a quantitative measure, the level of fine tuning must be less than some fixed amount, taken there to be the arbitrary threshold of 10%.
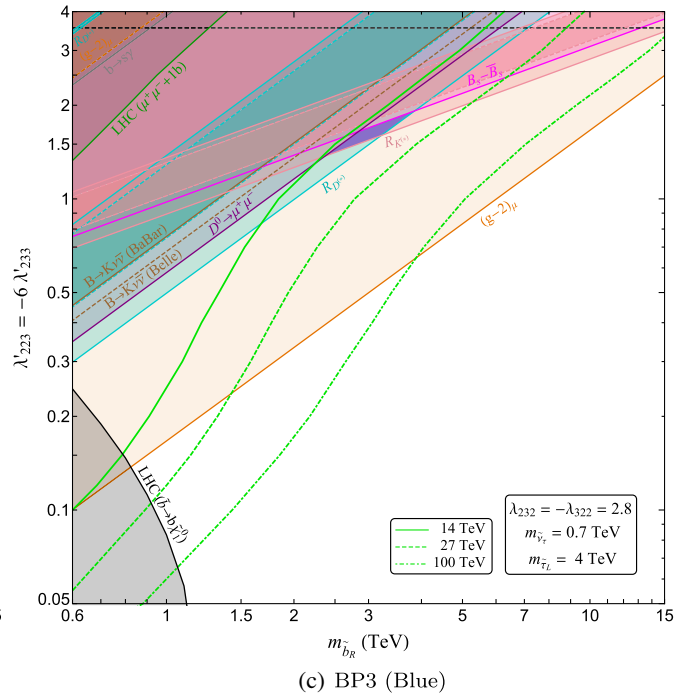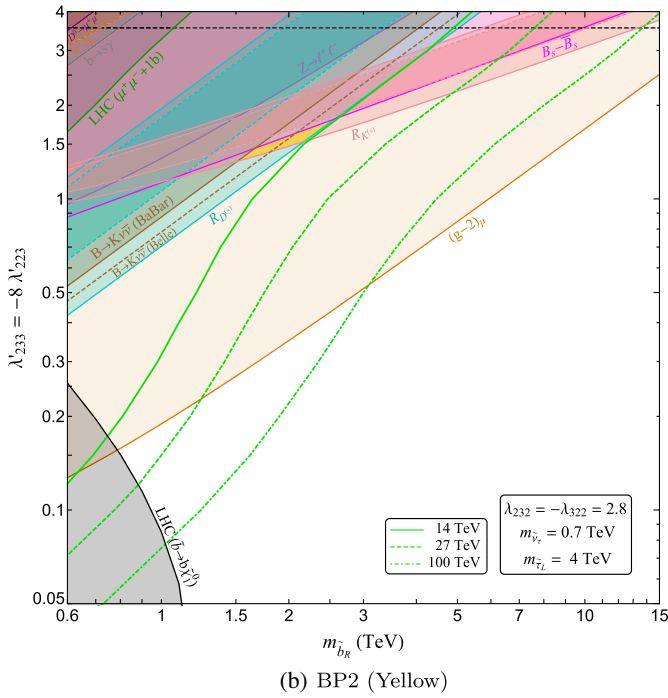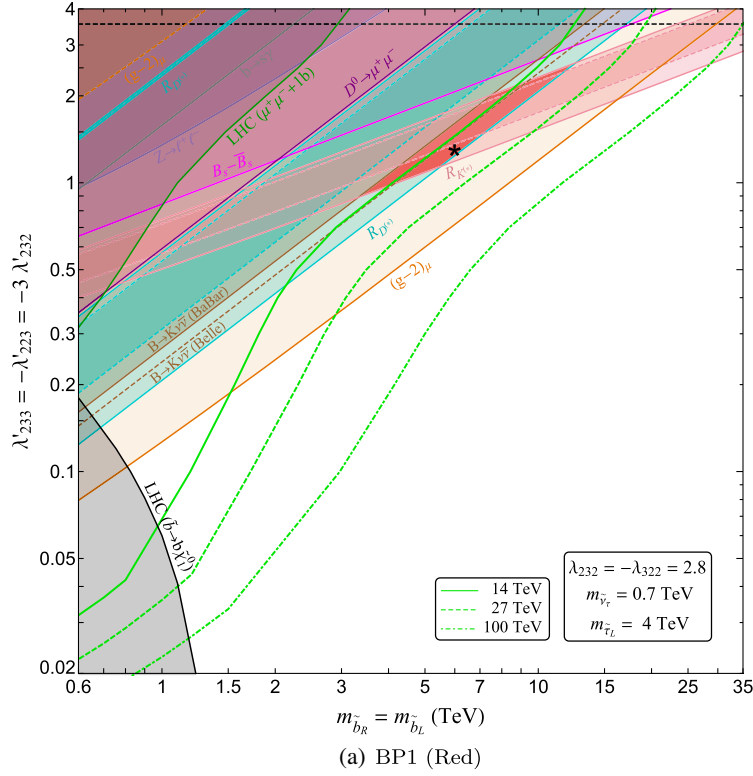
(a) BP1 (Red)

(b) BP2 (Yellow)

(c) BP3 (Blue)

FIG. 5. Three RPV3 benchmark cases in the $(m_{\tilde{b}_R}, \lambda'_{233})$ parameter space explaining the flavor anomalies. The cyan, pink and orange shaded regions with solid (dashed) boundaries explain the $R_{D^{(*)}}$, $R_{K^{(*)}}$ and $(g-2)_\mu$ anomalies at 3σ (2σ) respectively. The black-shaded region is excluded by the current LHC search for sbottoms in the bottom $+$ neutralino channel, whereas the dark green-shaded region is the LHC exclusion derived from a $\mu^+\mu^- + 1b$ search. The horizontal dotted line shows the perturbativity limit of $\sqrt{4\pi}$. Other shaded regions show the relevant low-energy flavor constrains on the parameter space from $B \to K\nu\bar{\nu}$ (brown), $B_s - \bar{B}_s$ mixing (magenta), $D^0 \to \mu^+\mu^-$ (purple), $b \to s\gamma$ (gray), and $Z \to \ell^+\ell^-$ (violet). The allowed overlap regions simultaneously explaining the $R_{D^{(*)}}$, $R_{K^{(*)}}$ and $(g-2)_\mu$ anomalies are shown by the red (top), yellow (bottom left), and blue (bottom right) shaded regions for the three benchmark cases. The $*$ mark on the top panel gives representative values of $m_{\tilde{b}_R}$ and λ'_{233} in the BP1 scenario that are used in Fig. 6. The green solid, dashed and dot-dashed contours respectively show the 2σ sensitivities of the 14 TeV LHC, 27 TeV, and 100 TeV pp colliders in the $\bar{t}\mu^+\mu^-$ channel discussed in the text.
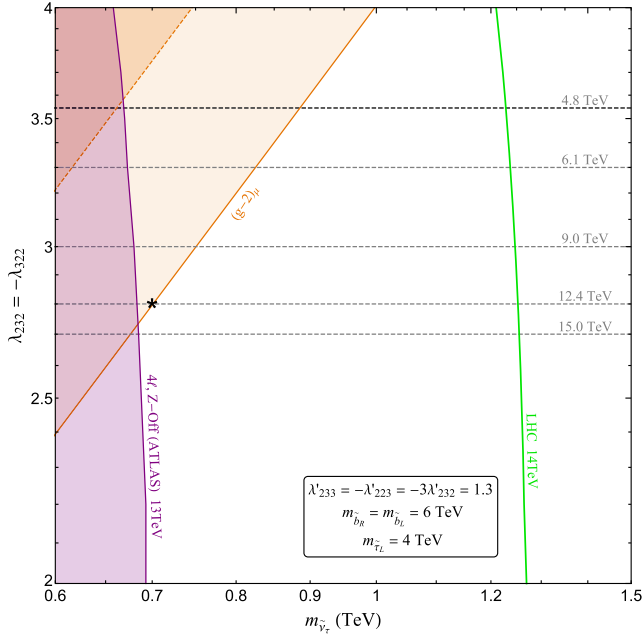
FIG. 6. The $(g-2)_\mu$-preferred region (orange-shaded) of the $(m_{\tilde{\nu}_\tau}, \lambda_{232})$ parameter space. The purple-shaded region is excluded by a 13 TeV LHC multilepton search [97], whereas the green curve is the 14 TeV HL-LHC sensitivity. The horizontal (gray) dashed lines show the positions of the Landau pole for given λ couplings and the black dashed line shows the perturbativity limit. The * gives representative values of $m_{\tilde{\nu}_\tau}$ and λ_{232} used in Fig. 5.

We should also comment on the $B_s - \bar{B}_s$ mixing constraint. For our benchmark points, the last term in Eq. (A2) does not contribute, as both λ'_{332} and λ'_{323} are set to zero.[8] For BP1 with $\lambda'_{223}/\lambda'_{232} = 3 \simeq -P_1^{LR}/P_1^{VLL}$, there is a cancellation (at the level of 5%) between the other two terms in Eq. (A2), thus enabling us to explain $R_{K^{(*)}}$ within 1σ, while this is not the case in BP2 and BP3 where $R_{K^{(*)}}$ can only be explained at 3σ level. Note that one can always assume a nonzero λ'_{232} for BP2 and BP3 [corresponding to the yellow and blue points out of the vertical axis in Figs. 4(b) and 4(c)] to make $B_s - \bar{B}_s$ mixing constraint weaker and enlarge the allowed parameter space for $R_{K^{(*)}}$, but this makes the $B \to K\nu\bar{\nu}$ constraint stronger, which limits the allowed region in BP2.

Our fit results for the best-case scenario are shown in Figs. 5 and 6 for the mutually orthogonal parameter spaces of $(m_{\tilde{b}_R}, \lambda')$ and $(m_{\tilde{\nu}_\tau}, \lambda)$ respectively. In Fig. 5, the cyan, pink, and orange-shaded regions with solid (dashed)

---

[8]As discussed before, a nonzero λ'_{3ij} combined with λ_{232} and light tau-sneutrino propagator will lead to strong tree-level meson decays $\bar{d}_i d_j \to \mu^+ \mu^-$. The excellent agreement between the experimental measurement [100] and SM prediction [101] of $\mathrm{BR}(B_s^0 \to \mu^+ \mu^-)$ requires an almost zero last term in Eq. (A2).

boundaries explain the $R_{D^{(*)}}$, $R_{K^{(*)}}$, and $(g-2)_\mu$ anomalies respectively at 3σ (2σ) CL The black-shaded region is the 13 TeV LHC exclusion derived from a sbottom search in the bottom + neutralino channel [96]. The dark-green-shaded region is the 13 TeV LHC exclusion derived from a $\mu^+\mu^- + 1b$ search [102] that is also applicable to our RPV3 scenario (see Sec. V). The horizontal dashed line shows the perturbativity limit of $\sqrt{4\pi}$. Other shaded regions in Fig. 5 show the relevant low-energy flavor constrains on the $(m_{\tilde{b}_R}, \lambda'_{233})$ parameter space from $B \to K\nu\bar{\nu}$ (brown), $B_s - \bar{B}_s$ mixing (magenta), $D^0 \to \mu^+\mu^-$ (purple), $b \to s\gamma$ (gray) and $Z \to \ell^+\ell^-$ (violet); see the Appendix for more details.

Now turning to the $(m_{\tilde{\nu}_\tau}, \lambda_{232})$ parameter space, the $(g-2)_\mu$-preferred region at 3σ (2σ) is shown by the solid (dashed) orange contours in Fig. 6. We have fixed the other RPV3 parameters using a benchmark point from the allowed region in Fig. 5 as shown by the * mark. The purple-shaded region is excluded by recasting the results of a recent 13 TeV LHC multilepton search [97], whereas the green curve is the 14 TeV HL-LHC sensitivity; see Sec. V. The horizontal black dashed line shows the perturbativity limit of $\sqrt{4\pi}$ as before. Because of the orthogonality between the $(m_{\tilde{b}_R}, \lambda')$ and $(m_{\tilde{\nu}_\tau}, \lambda)$ parameter spaces, the position of the * in Fig. 6 will not change much for BP2 and BP3; therefore, we do not include the corresponding figures for BP2 and BP3.

Since the required λ couplings are fairly large in our scenario, we also show the Landau pole positions by the horizontal gray dashed lines, which are obtained by numerically solving the relevant one-loop renormalization group equations (RGEs) [95]. Because the nonzero λ' couplings in our scenario do not couple to the third-generation slepton or sneutrino, the RGE for the λ_{232} coupling (and similarly, for the λ_{322} coupling) is very simple at one-loop level,

$$\frac{d}{dt}\lambda_{232} \simeq \frac{\lambda_{232}}{16\pi^2}\left(4\lambda_{232}^2 - \frac{9}{5}g_1^2 - 3g_2^2\right) \approx \frac{1}{4\pi^2}\lambda_{232}^3, \quad (11)$$

where g_1 and g_2 are the $U(1)_Y$ and $SU(2)_L$ gauge couplings, respectively, both of which are much smaller than the λ_{232} coupling in the parameter space shown in Fig. 6. We find that the benchmark point shown in Fig. 6 hits the Landau pole at 12.4 TeV.

One possible way out of the Landau pole issue is to consider a nonzero λ_{233} coupling instead of λ_{232}. This does not affect the $R_{D^{(*)}}$ and $R_{K^{(*)}}$ fit results presented in Fig. 5 because of the orthogonality between the λ' and λ parameter space mentioned before. As for the $(g-2)_\mu$-preferred region in the $(m_{\tilde{\nu}_\tau}, \lambda_{233})$ parameter space, the main difference with respect to Fig. 6 is that the allowed λ couplings can now be as low as 0.8, thus pushing the Landau pole to as high as 2.5×10^{16} GeV. The reason is that the relevant

LHC constraint for λ_{233} comes from $\mu^+\mu^-\tau^+\tau^-$ final state (in contrast with the $\mu^+\mu^-\mu^+\mu^-$ final state in Fig. 6). We did not find any 13 TeV LHC analysis in this channel, and using the old 8 TeV analysis from Ref. [103], we obtain a lower bound of only 150 GeV on the sneutrino mass. A dedicated 13 TeV analysis to update this bound is currently underway.

V. COLLIDER SIGNALS

Simple crossing-symmetry arguments have been used to establish high-p_T model-independent tests of the $R_{D^{(*)}}$ and $R_{K^{(*)}}$ anomalies in the CMS and ATLAS experiments [16,50,83,104–107]. The basic idea is that the underlying quark-level processes $b \to c\tau\nu$ for $R_{D^{(*)}}$ and $b \to s\ell^+\ell^-$ for $R_{K^{(*)}}$ necessarily imply, by crossing symmetry, the existence of processes like $pp \to \tau\nu$, $pp \to \ell^+\ell^-$, $pp \to b\tau\nu$, and $pp \to b\ell^+\ell^-$, which can be searched for in the high-p_T LHC experiments. In fact, a recent CMS study has found a mild discrepancy in the ratio of differential $\mu^+\mu^-$ to e^+e^- pair-production cross sections [108], which might turn out to be important for the $R_{K^{(*)}}$ anomaly. However, the model-independent effective field theory treatments relating the low-energy operators to the high-p_T LHC signals might break down, if the new physics cutoff scale is smaller than the LHC energies. Thus, it is important to explore all possible high-p_T LHC signals in the context of a given BSM scenario in order to distinguish it from other BSM interpretations of the flavor anomalies.

To this effect, we propose some striking LHC signals that could be used as an independent probe of the allowed RPV3 parameter space shown in Figs. 5 and 6 at the high-p_T LHC and future colliders. For the $(m_{\tilde{b}_R}, \lambda')$ parameter space in Fig. 5, we propose the process $pp \to \bar{t}(t)\mu^+\mu^-$ mediated by an sbottom (see Fig. 7). There is no $pp \to \bar{t}(t)\mu^+\mu^-$ final state in the SM, so the dominant SM background comes from $pp \to \bar{t}(t)\mu^+\mu^-X$ where X can be either a light jet (j), b-jet, or a gauge boson decaying to jets or leptons, which are somehow missed in the detector. We perform a parton-level simulation for the signal and background processes using MADGRAPH5_AMC@NLO v2.7.0 [109]. We assume that the (anti)top quark can be identified from its decay products and use the minimal

trigger cuts $p_T^{t,\mu} > 20$ GeV, $|\eta^{t,\mu}| < 2.5$, $\Delta R^{\mu\mu} > 0.4$, and $\Delta R^{t\mu} > 0.4$ for the $t(\bar{t})\mu^+\mu^-X$ final states. To estimate the SM background, we further require that the X containing jets, leptons or missing transverse energy is soft enough to evade detection, i.e., $p_T^{j,b,\ell} < 20$ GeV and $\not{E}_T < 20$ GeV.

For the RPV3 signal, we use the three benchmark points discussed in the previous section. It is easy to see that the $pp \to t\mu^+\mu^-$ and $pp \to \bar{t}\mu^+\mu^-$ give similar cross sections for the signal, because in all three cases, $\lambda'_{k13} = 0$, and therefore, the first-generation quarks do not participate in the initial state. For our parameter choice, the main contribution comes from $\bar{c}(c)g$ initial states as shown in Fig. 7. Since the $\bar{c}$ and c contents in proton are very similar, the resulting cross section should also be the same. However, for the SM background, $t\mu^+\mu^-X$ final state has two times more background than $\bar{t}\mu^+\mu^-X$, which mainly comes from the fact that the u content in proton is much larger than the $\bar{u}$ content. Therefore, we will only consider the $pp \to \bar{t}\mu^+\mu^-$ final state to show our sensitivity contours.

With the basic trigger cuts, we find that the total SM background for the $pp \to \bar{t}\mu^+\mu^-(+X)$ final state at $\sqrt{s} = 14$ TeV is 0.4 fb, which is dominated by $X = j$. For comparison, the corresponding signal cross section for the * point in BP1 in Fig. 5 is only 1.5×10^{-3} fb. However, we can improve the signal-to-background ratio substantially by using their different kinematic features. First of all, the $\mu^+\mu^-$ in the SM background case mainly comes from Z decay, so we expect the dimuon invariant mass $M_{\mu^+\mu^-}$ to peak at the Z-mass and to drop significantly at higher masses [see Fig. 8 (green)]. On the other hand, in our RPV3 case, one of the muons in the final state comes from sbottom decay, so we expect a longer tail in the $M_{\mu^+\mu^-}$ distribution, as confirmed in Fig. 8 (red). Therefore, using an appropriate cut on $M_{\mu^+\mu^-} > 400$ GeV, we can maximize the signal-to-background ratio. We find that the corresponding signal at the * point in BP1 and background cross sections after the $M_{\mu^+\mu^-}$ cut are respectively 1.1×10^{-3} fb and 4.2×10^{-4} fb. Further improvements in the signal-to-background can in principle be achieved using the fact that for an on shell sbottom decaying to $\bar{t}\mu^+$, we expect a peak at the sbottom mass in the invariant mass $M_{\bar{t}\mu^+}$ distribution for
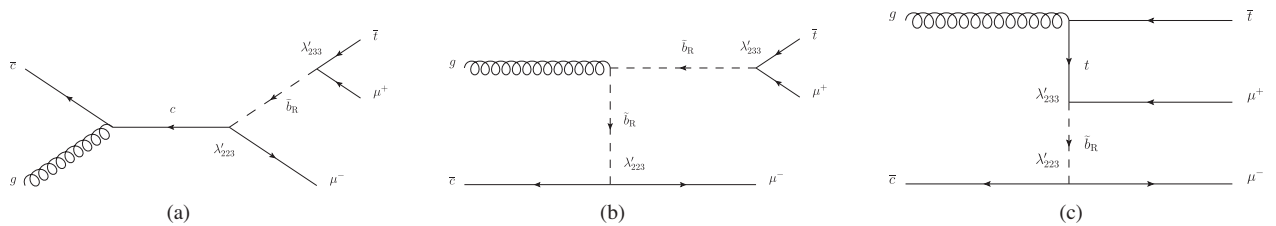

FIG. 7. Representative Feynman diagrams for the signal process $pp \to \bar{t}\mu^+\mu^-$. There are similar diagrams for the process $pp \to t\mu^+\mu^-$, however the SM background is larger for top-quark final states, compared to the antitop, so we only consider the latter case for drawing the sensitivity contours in Fig. 5.
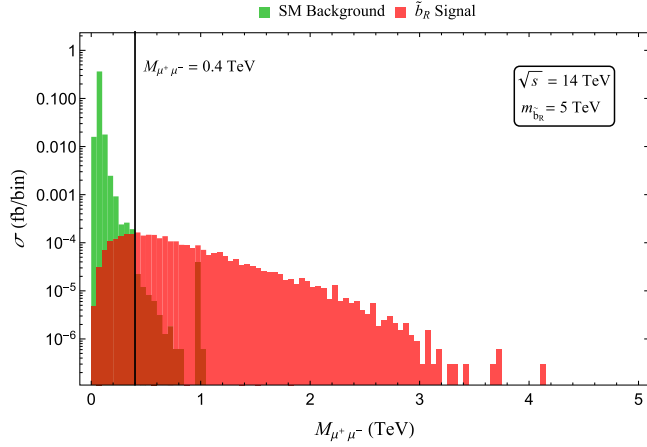
FIG. 8.   Dimuon invariant mass distribution for the RPV3 signal at the * point in BP1 (red) and SM background (green) in the $pp \to \bar{t}\mu^+\mu^-$ channel at 14 TeV LHC.
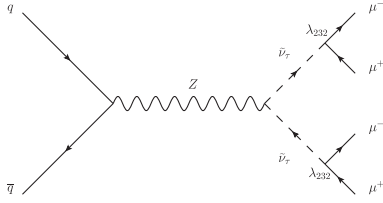

FIG. 9.   Feynman diagram for the four-lepton signal from the sneutrino pair production in our RPV3 model.

the signal, but not for the background. However, since the final-state reconstruction involving top quarks is somewhat involved, especially for the leptonic decay of the W boson coming from the top, and also the sbottom mass is not known *a priori* (we use it as a free parameter in Fig. 5), we refrain from using the $M_{\bar{t}\mu^+}$ cut in our analysis.

Assuming an integrated luminosity of $\mathcal{L} = 3000$ fb^{-1}, we show the 2σ signal significance in Fig. 5 by the green solid, dashed and dot-dashed contours for $\sqrt{s} = 14$, 27 and 100 TeV colliders, respectively. We find that a portion of the overlap region explaining all flavor anomalies can already be accessed at the HL-LHC, while the proposed future colliders should be able to access the entire allowed parameter space.

Now for the $(m_{\tilde{\nu}_\tau}, \lambda)$ parameter space in Fig. 6 relevant only for the $(g-2)_\mu$ anomaly, we focus on the spectacular four-muon final state [110] coming from the sneutrino pair production, followed by each sneutrino decaying into two muons via the λ_{232} coupling (see Fig. 9). Such multilepton channels are very clean even at the hadron colliders, and in fact, the results of a recent ATLAS multilepton analysis [97] can already be recast into a new bound on the sneutrino mass. Using the 95% CL observed cross section limit of 0.044 fb for the 4ℓ, off-Z signal region with

$M_{4\mu} > 400$ GeV[9] and the same selection criteria as in Ref. [97], we obtain a lower bound of $m_{\tilde{\nu}_\tau} \gtrsim 670$ GeV, as shown by the purple-shaded region in Fig. 6. This LHC constraint already rules out a big chunk of the $(g-2)_\mu$-preferred region and pushes the λ_{232} coupling toward the perturbativity limit. The HL-LHC can completely cover the remaining $(g-2)_\mu$-preferred region, as shown by the green curve in Fig. 6.

VI. DISCUSSION

In this section, we make a few remarks on our results before concluding our discussion.

A. Interplay between anomalies

We find in Fig. 6 that only a narrow region in the $(m_{\tilde{\nu}}, \lambda_{232})$ parameter space is allowed that could explain the $(g-2)_\mu$ anomaly in our minimal RPV3 setup. It is worth checking how does the $(g-2)_\mu$-preferred region gets affected on its own, and more importantly, if dropping the $R_{D^{(*)}}$ and $R_{K^{(*)}}$ anomalies could open up more parameter space in Figs. 2 and 6. To this effect, we find that allowing $\lambda'_{213} \neq 0$ in Eq. (8), the $(g-2)_\mu$ solution can be improved only slightly, compared to Fig. 6. With $m_{\tilde{b}_R} = 1.23$ TeV (the minimum value allowed by LHC 13 TeV data) and $|\lambda'_{233}| = 1.57$ (the maximum value allowed from the Z-decay universality constraint g_A^μ/g_A^e, where g_A^ℓ is the axial-vector coupling of Z to leptons), the lower 3σ bound of $(g-2)_\mu$ starts at (0.7 TeV, 2.66) and ends at (0.93 TeV, $\sqrt{4\pi}$) in the $(m_{\tilde{\nu}_\tau}, \lambda_{232})$ parameter space. The lower 2σ bound is still not reached for $\lambda_{232} < \sqrt{4\pi}$. Because of the constraints $B \to K\nu\bar{\nu}$ and $K \to \pi\nu\bar{\nu}$, $\lambda'_{213}, \lambda'_{223} \approx 0$ and thus cannot contribute much to the $(g-2)_\mu$ anomaly in this optimal $(g-2)_\mu$ case.

Nevertheless, it is important to mention that due to the orthogonality between $(m_{\tilde{\nu}_\tau}, \lambda)$ and $(m_{\tilde{b}_R}, \lambda')$ parameter spaces in our RPV3 scenario, even if the four-muon signal completely rules out the $(g-2)_\mu$-favored region in Fig. 6 [drawn for BP1, but similar for BP2 and BP3 as we can see from Fig. 4(i)], the $R_{D^{(*)}}$ and $R_{K^{(*)}}$ anomalies can still be explained by the $(m_{\tilde{b}_R}, \lambda')$ parameter space shown in Fig. 5. Similarly, suppose the $pp \to \bar{t}\mu^+\mu^-$ signal completely rules out one of the overlap regions in Fig. 5, but it will not affect the $(g-2)_\mu$ solution in Fig. 6.

B. Leptoquark versus RPV3

Several BSM scenarios have been invoked to explain the flavor anomalies, but very few have the ability to explain all the flavor anomalies simultaneously in a minimal, theoretically well-motivated setup like the RPV3. Leptoquarks

---

[9]This also removes potential contributions from heavy neutral Higgs to ZZ final states.

(LQs) have been a popular choice, but a single scalar LQ solution has now been disfavored by global fits [111]. A single vector LQ $U_1(\mathbf{3},\mathbf{1},2/3)$ still remains a viable option [112–114], but must be embedded in some ultraviolet completion like the Pati-Salam gauge group [115–117], thus necessarily requiring more particles to cancel gauge anomalies, and hence, losing its minimality feature. Another alternative is to invoke more than one scalar LQs [118–123]. The right-sbottom with λ' couplings in our RPV3 scenario behaves exactly like the $SU(2)_L$-singlet LQ $S_1(\mathbf{3},\mathbf{1},-1/3)$ originally invoked in Ref. [124], which still gives an excellent fit to the $b \to c\tau\nu$ data, including polarization observables and forward-backward asymmetry [125]. However, the same S_1 LQ cannot explain the $b \to s\mu^+\mu^-$ data simultaneously [126], while being consistent with the low-energy constraints, in particular from $B_s - \bar{B}_s$ mixing. This is a key difference with RPV3, where a TeV-scale sbottom by itself can explain both $R_{D^{(*)}}$ and $R_{K^{(*)}}$, owing to a (partial) cancellation in the $B_s - \bar{B}_s$ mixing [c.f. Eq. (A2)]. Another important difference is the λ coupling, which gives rise to the distinct four-lepton signal in the RPV3 scenario and uniquely distinguishes our scenario from LQ models.

C. Precision tests

Apart from the collider tests proposed here, our RPV3 solution to the flavor anomalies can also be probed via low-energy precision observables at LHCb and Belle-II. For instance, the * benchmark point in Fig. 5 predicts the ratio [c.f. Eq. (A1)] $R_{B \to K\nu\bar{\nu}} = 2.1$, which is just below the Belle 95% CL upper limit of 3.2 [127,128]. The future Belle-II sensitivity can improve this limit by up to a factor of 5 [129], which should be able to completely probe the overlap region. In particular, the red, yellow, and blue overlap regions in Fig. 5 can be completely excluded for $R_{B \to K\nu\bar{\nu}} < 1.7$, 2.0, and 1.1 respectively. This is a distinct feature of our RPV3 scenario.[10] Similarly, future lattice improvements in the precision of the SM prediction for $B_s - \bar{B}_s$ mixing could be fateful for the overlap region in Fig. 5. In addition, hints of LFUV in other independent observables involving the third generation, such as LFV τ and B decays, $b \to c\mu\nu/b \to ce\nu$ and baryonic decay modes like $\Lambda_b \to \Lambda\ell^+\ell^-$, would provide critical further tests of our proposal. Furthermore, there are other lepton flavor violating B and τ decays that could get enhanced contributions from RPV3 within reach of Belle II sensitivity [16]. If the flavor anomalies persist and grow in statistical significance, the precision flavor observables mentioned above, in conjunction with the collider observables discussed in Sec. V, might be able to uniquely distinguish our RPV3 interpretation from other BSM interpretations.

---

[10]For instance, in the U_1 vector LQ case, there is no tree-level contribution to $B \to K\nu\bar{\nu}$ and any prediction involving loop processes depends on the UV-completion details.

D. Caveats

In spite of all the above mentioned attractive features of our RPV3 scenario, there are a few weak points which we just lay out here for future contemplation.

(a) *Landau Pole*: In the minimal RPV3 setup presented here, some of the λ' and λ couplings are required to be fairly large $\gtrsim \mathcal{O}(1)$. Such large couplings would hit the Landau pole very quickly, preventing the model from being valid all the way up to the gauge coupling unification scale. For instance, the benchmark point shown in Fig. 6 hits the Landau pole at 12.4 TeV. There might be a way out in the general RPV-MSSM with more parameters, but a detailed analysis of the full MSSM parameter space is beyond the scope of this work.

(b) *Neutrino Mass*: The trilinear RPV couplings in Eqs. (1) and (2) contribute to neutrino masses at one-loop level through the lepton-slepton and quark-squark loops [54,130,131]. To ensure that the neutrino masses remain small and satisfy the cosmological bound on the sum $\sum_i m_{\nu_i} \lesssim 0.1$ eV [132], we require some degree of cancellation between the soft trilinear A terms and the $\mu \tan\beta$ term [16], depending on the other SUSY parameters.

(c) *Dark Matter*: In RPV scenarios, the lightest supersymmetric particle (LSP) is no longer stable, but decays to SM particles. Therefore, it cannot be the dark matter of the Universe, unless it is sufficiently long-lived, which requires extremely small values of the RPV couplings. In our RPV3 scenario with $\mathcal{O}(1)$ RPV couplings, the neutralino LSP cannot be the dark matter. However, a gravitino LSP with its naturally Planck-suppressed decays can in principle have a lifetime much longer than the age of the Universe, and hence, be the dark matter [133].

(d) *Hierarchy of RPV Couplings*: For our numerical analysis, we have treated the relevant RPV couplings as free parameters and find the best-fit that explains the flavor anomalies. We find that some of the RPV couplings need to be fairly large $\gtrsim \mathcal{O}(1)$, while some others need to be hierarchically smaller, and yet others need to be extremely small or vanishing. One could in principle invoke a flavor symmetry (similar to Ref. [68] for instance) to explain such hierarchy between couplings; so this need not be an insurmountable issue, although it would require further work.

VII. CONCLUSION

The flavor anomalies might already be giving us the first glimpse of natural supersymmetry with light third-generation sfermions and with R-parity violating couplings. We have proposed a simple, testable RPV3 scenario that simultaneously explains the $R_{D^{(*)}}$, $R_{K^{(*)}}$, and $(g-2)_\mu$

anomalies with TeV-scale sbottom and tau sneutrino which are easily accessible at the HL-LHC. With experimental updates from LHCb, Belle-II, and Fermilab muon $(g-2)$ experiments in the next few years, as well as with better limits on third-generation sfermion masses from the LHC, our knowledge of the anomalies will surely evolve and the allowed RPV3 ranges shown in Figs. 5 and 6 may have to be modified accordingly. But let us hope SUSY prevails in the end.

APPENDIX: LOW-ENERGY CONSTRAINTS

Despite the many free parameters our RPV3 scenario is remarkably well constrained by various low-energy flavor observables so much so that more accurate measurements of $R_{D^{(*)}}$, $R_{K^{(*)}}$ and $(g-2)_\mu$ preserving the central values could have appreciable adverse consequences on our RPV3 explanation of these anomalies. In this section, we summarize all relevant constraints on our RPV3 scenario shown in Fig. 5. For more details and additional constraints (which are weaker, and therefore not mentioned here) see Ref. [16].

1. $B \to K^{(*)}\nu\bar{\nu}$

As shown in Fig. 10, $B \to K^{(*)}\nu\bar{\nu}$ receives a tree-level RPV3 contribution via sbottom exchange. The branching ratio is given by
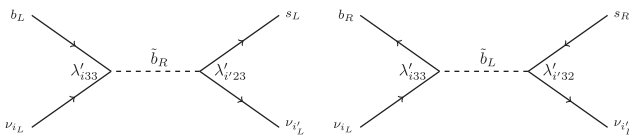

FIG. 10. Contributions to $B \to K^{(*)}\nu\bar{\nu}$ via λ' interactions in RPV3.

$$R_{B \to K^{(*)}\nu\bar{\nu}} \equiv \frac{\mathrm{BR}(B \to K^{(*)}\nu\bar{\nu})}{\mathrm{BR}(B \to K^{(*)}\nu\bar{\nu})_{\mathrm{SM}}}$$
$$= \frac{1}{3}\left|\delta_{ii'} - \frac{v^2\pi s_w^2}{2\alpha_{\mathrm{em}}}\frac{\lambda'_{i33}}{V_{tb}V_{ts}^*}\left(\frac{\lambda'_{i'23}}{m_{\tilde{b}_R}^2} + \frac{\lambda'_{i'32}}{m_{\tilde{b}_L}^2}\right)\frac{1}{X_t}\right|^2. \tag{A1}$$

with the top loop function $X_t = 1.469 \pm 0.017$ [134] and s_w being the weak mixing angle. We consider both $\tilde{b}_L$ and $\tilde{b}_R$ exchanges assuming that $m_{\tilde{b}_L} = m_{\tilde{b}_R}$ for numerical purposes. An experimental upper bound for this ratio exists; $R_{B \to K^{(*)}\nu\bar{\nu}} < 5.2$ at 95% CL [135,136], which was adopted for our original parameter setting and indicated in Fig. 5 as the solid brown line. However, stronger upper bounds of $R_{B \to K\nu\bar{\nu}} < 3.9$ and $R_{B \to K^*\nu\bar{\nu}} < 2.7$ have been quoted by Belle but at 90% CL [127]. In order to make a fair comparison with the other low-energy and collider bounds which are all given at 95% CL, we have derived an approximate 95% CL equivalent bound using the Belle data provided in Ref. [127]. We get $R_{B \to K^*\nu\bar{\nu}} \lesssim 3.2$, where we have used the theoretical uncertainty from Ref. [128] and have also taken into account the propagation of uncertainty. This 95% CL upper limit is shown in Fig. 5 by the dashed brown line.

2. $B_s - \bar{B}_s$ Mixing

Experimentally, the mass difference ΔM_{B_s} in neutral B_s meson mixing is measured with excellent precision, $\Delta M_{B_s} = (17.757 \pm 0.021)\ \mathrm{ps}^{-1}$ [13], dominated by LHCb and still statistically limited. On the other hand, the SM prediction $\Delta M_{B_s}^{\mathrm{SM}} = (19.3 \pm 1.7)\ \mathrm{ps}^{-1}$ [16,137] has sizable uncertainties stemming mainly from the hadronic matrix elements and the CKM matrix element V_{cb}.

In RPV3, additional contributions can arise at the tree level from sneutrino exchange, or at the one-loop level from box diagrams with sbottoms, sneutrinos, or stops (see Fig. 11). For the mass difference, we obtain
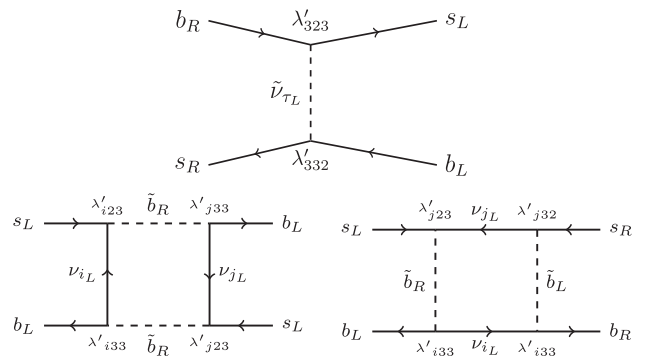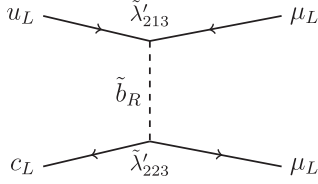

FIG. 11. Relevant contributions to $B_s - \bar{B}_s$ mixing via λ' couplings in RPV3.

FIG. 12. Contribution to $D^0 \to \mu^+\mu^-$ from λ' in RPV3.

$$\Delta M_{B_s}^{\rm RPV} = \frac{2}{3} m_{B_s} f_{B_s}^2 \left| P_1^{VLL} \frac{\lambda'_{i23}\lambda'_{j33}\lambda'_{j23}\lambda'_{i33}}{128\pi^2 m_{\tilde{b}_R}^2} \right.$$

$$\left. + P_1^{LR} \frac{\lambda'_{i23}\lambda'_{j33}\lambda'_{i32}\lambda'_{j33}}{128\pi^2 m_{\tilde{b}_R} m_{\tilde{b}_L}} + P_2^{LR} \frac{\lambda'_{332}\lambda'_{323}}{2m_{\tilde{\nu}}^2} \right|, \quad (A2)$$

where

$$P_1^{VLL} = 0.80, \quad P_1^{LR} = -2.52 \text{ and } P_2^{LR} = 3.08, \quad (A3)$$

are the updated hadronic P factors from Ref. [138] with the latest lattice input from Ref. [139] (see also Refs. [140,141]), $f_{B_s} = (274 \pm 8)$ MeV is the B_s decay constant, and i, j are neutrino-flavor indices in the box graphs. Combining our SM prediction with the experimental result we obtain the following bound at 95% CL on

$$0.78 < \left| \frac{\Delta M_{B_s}}{\Delta M_{B_s}^{\rm SM}} \right| < 1.12, \quad (A4)$$

which constrains the RPV3 contribution in Eq. (A2). This bound is indicated as the magenta-shaded region in Fig. 5.

3. $D^0 \to \mu^+\mu^-$

As shown in Fig. 12, there is a tree-level contribution from sbottom exchange to this rare D^0 decay width which can be expressed as

$$\Gamma(D^0 \to \mu^+\mu^-) = \frac{1}{128\pi} \left| \frac{\lambda'_{2j3}\lambda'_{2j'3} V_{uj'} V_{cj}}{m_{\tilde{b}_R}^2} \right|^2 f_D^2$$

$$\times m_D m_\mu^2 \sqrt{1 - 4m_\mu^2/m_D^2}, \quad (A5)$$

where $f_D = (212 \pm 1)$ MeV is the D^0 decay constant. Using the experimental upper bound on this branching ratio [142] of 7.6×10^{-9} at 95% CL, we calculate the corresponding bound on the RPV3 parameter space, as shown by the purple-shaded region in Fig. 5.

4. $Z \to \ell\bar{\ell}'$

This process gets modified by top-sbottom loops, as shown in Fig. 13. A change in the Z decay from the SM prediction will affect the ratios of the vector and
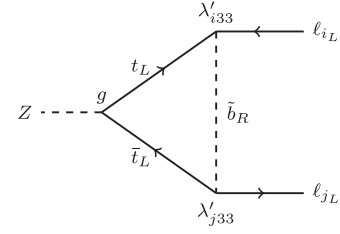
FIG. 13. Contribution to $Z \to \ell\bar{\ell}'$ from λ' in RPV3.

axial-vector couplings of the Z boson with different lepton flavors. Experimental measurements on these couplings are [91]

$$\left(\frac{g_V^\tau}{g_V^e} \right)_{\rm exp} = 0.9588 \pm 0.02997, \quad (A6)$$

$$\left(\frac{g_A^\tau}{g_A^e} \right)_{\rm exp} = 1.0019 \pm 0.00145. \quad (A7)$$

The contributions to these ratios from RPV3 are given by

$$\left(\frac{g_V^\tau}{g_V^e} \right)_{\rm SM+RPV} = 1 - \frac{2\delta g_{\ell_3\ell_3}}{1 - 4s_w^2},$$

$$\left(\frac{g_A^\tau}{g_A^e} \right)_{\rm SM+RPV} = 1 - 2\delta g_{\ell_3\ell_3},$$

where

$$\delta g_{\ell_i\ell_j} \simeq \frac{3y_t^2}{32\sqrt{2}G_F\pi^2} \frac{\lambda'_{i33}\lambda'_{j33}}{m_{\tilde{b}_R}^2} \left[\log\left(\frac{m_{\tilde{b}_R}}{m_Z} \right) - 0.612 \right]. \quad (A8)$$

Taking i, j both equal to 3 and using Eqs. (A6) and (A7), we derive a bound on the RPV3 parameter space, as shown by the violet-shaded region in Fig. 5.
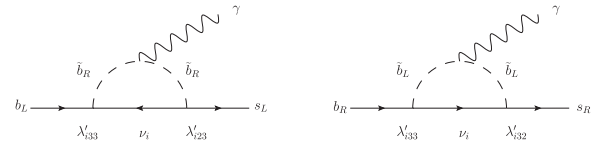
5. $b \to s\gamma$

The branching ratio of $b \to s\gamma$ has been measured [13] as

$$\text{BR}(b \to s\gamma)_{\rm exp} = (3.43 \pm 0.21 \pm 0.07) \times 10^{-4}, \quad (A9)$$

which is consistent with SM [143],

$$\text{BR}(b \to s\gamma)_{\rm SM} = (3.36 \pm 0.23) \times 10^{-4}. \quad (A10)$$

FIG. 14. Contribution to $b \to s\gamma$ from λ' couplings in RPV3.

In RPV3, there are one-loop contributions involving both left- and right-handed sbottoms (see Fig. 14). Comparing this to the difference between the experimental and SM results, we obtain the following bound at 95% C.L.,

$$|\lambda'_{223}\lambda'_{233}| \lesssim 0.025 \left(\frac{100 \text{ GeV}}{m_{\tilde{b}_R}}\right)^{-2}, \qquad \text{(A11)}$$

$$|\lambda'_{232}\lambda'_{233}| \lesssim 0.01 \left(\frac{100 \text{ GeV}}{m_{\tilde{b}_L}}\right)^{-2}. \qquad \text{(A12)}$$

This is shown by the gray shaded region in Fig. 5.

[1] O. Fischer *et al.*, arXiv:2109.06065.

[2] J. P. Lees *et al.* (BABAR Collaboration), Phys. Rev. Lett. **109**, 101802 (2012).

[3] M. Huschle *et al.* (Belle Collaboration), Phys. Rev. D **92**, 072014 (2015).

[4] S. Hirose *et al.* (Belle Collaboration), Phys. Rev. Lett. **118**, 211801 (2017).

[5] A. Abdesselam *et al.* (Belle Collaboration), arXiv:1904.08794.

[6] A. Abdesselam *et al.* (Belle Collaboration), Phys. Rev. Lett. **126**, 161801 (2021).

[7] S. Choudhury *et al.* (BELLE Collaboration), J. High Energy Phys. 03 (2021) 105.

[8] R. Aaij *et al.* (LHCb Collaboration), Phys. Rev. Lett. **115**, 111803 (2015); **115**, 159901(E) (2015).

[9] R. Aaij *et al.* (LHCb Collaboration), Phys. Rev. Lett. **120**, 171802 (2018).

[10] R. Aaij *et al.* (LHCb Collaboration), J. High Energy Phys. 08 (2017) 055.

[11] R. Aaij *et al.* (LHCb Collaboration), Phys. Rev. Lett. **122**, 191801 (2019).

[12] R. Aaij *et al.* (LHCb Collaboration), Nat. Phys. **18**, 277 (2022).

[13] Y. S. Amhis *et al.* (HFLAV Collaboration), Eur. Phys. J. C **81**, 226 (2021).

[14] M. Bordone, G. Isidori, and A. Pattori, Eur. Phys. J. C **76**, 440 (2016).

[15] F. U. Bernlochner, Z. Ligeti, M. Papucci, and D. J. Robinson, Phys. Rev. D **95**, 115008 (2017); **97**, 059902 (E) (2018).

[16] W. Altmannshofer, P. S. B. Dev, A. Soni, and Y. Sui, Phys. Rev. D **102**, 015031 (2020).

[17] F. Jegerlehner and A. Nyffeler, Phys. Rep. **477**, 1 (2009).

[18] B. Abi *et al.* (Muon g-2 Collaboration), Phys. Rev. Lett. **126**, 141801 (2021).

[19] G. W. Bennett *et al.* (Muon g-2 Collaboration), Phys. Rev. D **73**, 072003 (2006).

[20] T. Aoyama *et al.*, Phys. Rep. **887**, 1 (2020).

[21] B. E. Lautrup, A. Peterman, and E. de Rafael, Phys. Rep. **3**, 193 (1972).

[22] A. Czarnecki, B. Krause, and W. J. Marciano, Phys. Rev. D **52**, R2619 (1995).

[23] A. Czarnecki, B. Krause, and W. J. Marciano, Phys. Rev. Lett. **76**, 3267 (1996).

[24] G. Colangelo, M. Hoferichter, and P. Stoffer, J. High Energy Phys. 02 (2019) 006.

[25] M. Benayoun, L. Delbuono, and F. Jegerlehner, Eur. Phys. J. C **80**, 81 (2020); **80**, 244(E) (2020).

[26] M. Hoferichter, B.-L. Hoid, and B. Kubis, J. High Energy Phys. 08 (2019) 137.

[27] M. Davier, A. Hoecker, B. Malaescu, and Z. Zhang, Eur. Phys. J. C **80**, 241 (2020); **80**, 410(E) (2020).

[28] A. Keshavarzi, D. Nomura, and T. Teubner, Phys. Rev. D **101**, 014029 (2020).

[29] T. Blum, Phys. Rev. Lett. **91**, 052001 (2003).

[30] Sz. Borsanyi, Z. Fodor, C. Hoelbling, T. Kawanai, S. Krieg, L. Lellouch, R. Malak, K. Miura, K. K. Szabo, C. Torrero, and B. C. Toth (Budapest-Marseille-Wuppertal Collaboration), Phys. Rev. Lett. **121**, 022002 (2018).

[31] T. Blum, P. A. Boyle, V. Guelpers, T. Izubuchi, L. Jin, C. Jung, A. Juettner, C. Lehner, A. Portelli, and J. T. Tsang (RBC, UKQCD Collaborations), Phys. Rev. Lett. **121**, 022003 (2018).

[32] D. Giusti, V. Lubicz, G. Martinelli, F. Sanfilippo, and S. Simula, Phys. Rev. D **99**, 114502 (2019).

[33] E. Shintani and Y. Kuramashi (PACS Collaboration), Phys. Rev. D **100**, 034517 (2019).

[34] C. T. H. Davies *et al.* (Fermilab Lattice, LATTICE-HPQCD, MILC Collaborations), Phys. Rev. D **101**, 034512 (2020).

[35] A. Gérardin, M. Cè, G. von Hippel, B. Hörz, H. B. Meyer, D. Mohler, K. Ottnad, J. Wilhelm, and H. Wittig, Phys. Rev. D **100**, 014510 (2019).

[36] S. Borsanyi *et al.*, Nature (London) **593**, 51 (2021).

[37] C. Lehner and A. S. Meyer, Phys. Rev. D **101**, 074515 (2020).

[38] Y. Shamir, Phys. Lett. B **305**, 357 (1993).

[39] V. Furman and Y. Shamir, Nucl. Phys. **B439**, 54 (1995).

[40] T. Blum and A. Soni, Phys. Rev. D **56**, 174 (1997).

[41] T. Blum and A. Soni, Phys. Rev. Lett. **79**, 3595 (1997).

[42] C. W. Bernard, T. Draper, A. Soni, H. D. Politzer, and M. B. Wise, Phys. Rev. D **32**, 2343 (1985).

[43] W.-J. Lee and S. R. Sharpe, Phys. Rev. D **60**, 114503 (1999).

[44] C. Aubin and C. Bernard, Phys. Rev. D **68**, 034014 (2003).

[45] C. Aubin and C. Bernard, Phys. Rev. D **68**, 074011 (2003).

[46] A. Crivellin, M. Hoferichter, C. A. Manzari, and M. Montull, Phys. Rev. Lett. **125**, 091801 (2020).

[47] A. Keshavarzi, W. J. Marciano, M. Passera, and A. Sirlin, Phys. Rev. D **102,** 033002 (2020).

[48] E. de Rafael, Phys. Rev. D **102,** 056025 (2020).

[49] B. Malaescu and M. Schott, Eur. Phys. J. C **81,** 46 (2021).

[50] W. Altmannshofer, P. S. B. Dev, and A. Soni, Phys. Rev. D **96,** 095010 (2017).

[51] C. Brust, A. Katz, S. Lawrence, and R. Sundrum, J. High Energy Phys. 03 (2012) 103.

[52] H. Baer, V. Barger, P. Huang, and X. Tata, J. High Energy Phys. 05 (2012) 109.

[53] M. Badziak, E. Dudas, M. Olechowski, and S. Pokorski, J. High Energy Phys. 07 (2012) 155.

[54] R. Barbier, C. Bérat, M. Besançon, M. Chemtob, A. Deandrea, E. Dudas, P. Fayet, S. Lavignac, G. Moreau, E. Perez, and Y. Sirois, Phys. Rep. **420,** 1 (2005).

[55] C.-N. Yang and R. L. Mills, Phys. Rev. **96,** 191 (1954).

[56] M. Ablikim *et al.* (BESIII Collaboration), Phys. Rev. Lett. **121,** 171803 (2018).

[57] M. Ablikim *et al.* (BESIII Collaboration), Phys. Rev. Lett. **122,** 011804 (2019).

[58] M. Ablikim (BESIII Collaboration), Phys. Rev. D **101,** 072005 (2020).

[59] M. Ablikim (BESIII Collaboration), Phys. Rev. Lett. **124,** 231801 (2020).

[60] M. Ablikim *et al.* (BESIII Collaboration), Phys. Rev. D **104,** L091103 (2021).

[61] F. Ambrosino *et al.* (KLOE Collaboration), Eur. Phys. J. C **64,** 627 (2009); **65,** 703(E) (2010).

[62] C. Lazzeroni *et al.* (NA62 Collaboration), Phys. Lett. B **719,** 326 (2013).

[63] M. Ablikim *et al.* (BESIII Collaboration), Phys. Rev. Lett. **127,** 121802 (2021).

[64] M. Papucci, J. T. Ruderman, and A. Weiler, J. High Energy Phys. 09 (2012) 035.

[65] N. G. Deshpande and A. Menon, J. High Energy Phys. 01 (2013) 025.

[66] J. Zhu, H.-M. Gan, R.-M. Wang, Y.-Y. Fan, Q. Chang, and Y.-G. Xu, Phys. Rev. D **93,** 094023 (2016).

[67] N. G. Deshpande and X.-G. He, Eur. Phys. J. C **77,** 134 (2017).

[68] S. Trifinopoulos, Eur. Phys. J. C **78,** 803 (2018).

[69] Q.-Y. Hu, X.-Q. Li, Y. Muramatsu, and Y.-D. Yang, Phys. Rev. D **99,** 015008 (2019).

[70] S. Trifinopoulos, Phys. Rev. D **100,** 115022 (2019).

[71] D.-Y. Wang, Y.-D. Yang, and X.-B. Yuan, Chin. Phys. C **43,** 083103 (2019).

[72] S. Biswas, D. Chowdhury, S. Han, and S. J. Lee, J. High Energy Phys. 02 (2015) 142.

[73] D. Das, C. Hati, G. Kumar, and N. Mahajan, Phys. Rev. D **96,** 095033 (2017).

[74] K. Earl and T. Grégoire, J. High Energy Phys. 08 (2018) 201.

[75] Q.-Y. Hu and L.-L. Huang, Phys. Rev. D **101,** 035030 (2020).

[76] M.-D. Zheng and H.-H. Zhang, Phys. Rev. D **104,** 115023 (2021).

[77] J. E. Kim, B. Kyae, and H. M. Lee, Phys. Lett. B **520,** 298 (2001).

[78] L. E. Ibanez and G. G. Ross, Phys. Lett. B **260,** 291 (1991).

[79] L. E. Ibanez and G. G. Ross, Nucl. Phys. **B368,** 3 (1992).

[80] C. Murgui, A. Peñuelas, M. Jung, and A. Pich, J. High Energy Phys. 09 (2019) 103.

[81] J. P. Lees *et al.* (BABAR Collaboration), Phys. Rev. D **88,** 072012 (2013).

[82] M. T. Prim (Belle Collaboration), in 54th Rencontres de Moriond on Electroweak Interactions and Unified Theories (2019), pp. 297–296, arXiv:1906.06871.

[83] A. Greljo, J. Martin Camalich, and J. D. Ruiz-Alvarez, Phys. Rev. Lett. **122,** 131803 (2019).

[84] R. Alonso, B. Grinstein, and J. Martin Camalich, Phys. Rev. Lett. **118,** 081802 (2017).

[85] A. G. Akeroyd and C.-H. Chen, Phys. Rev. D **96,** 075011 (2017).

[86] J. Aebischer and B. Grinstein, J. High Energy Phys. 07 (2021) 130.

[87] S. Iguro, Phys. Rev. D **105,** 095011 (2022).

[88] W. Altmannshofer and P. Stangl, Eur. Phys. J. C **81,** 952 (2021).

[89] W. Altmannshofer and D. M. Straub, Eur. Phys. J. C **73,** 2646 (2013).

[90] W. Altmannshofer and D. M. Straub, Eur. Phys. J. C **75,** 382 (2015).

[91] P. A. Zyla *et al.* (Particle Data Group), Prog. Theor. Exp. Phys. **2020,** 083C01 (2020).

[92] T. Moroi, Phys. Rev. D **53,** 6565 (1996); **56,** 4424(E) (1997).

[93] A. Czarnecki and W. J. Marciano, Phys. Rev. D **64,** 013014 (2001).

[94] S. Baum, M. Carena, N. R. Shah, and C. E. M. Wagner, J. High Energy Phys. 01 (2022) 025.

[95] B. C. Allanach, A. Dedes, and H. K. Dreiner, Phys. Rev. D **60,** 056002 (1999); **86,** 039906(E) (2012).

[96] A. M. Sirunyan *et al.* (CMS Collaboration), Phys. Lett. B **778,** 263 (2018).

[97] ATLAS-CONF-2021-011 (2021).

[98] M. R. Buckley, D. Feld, S. Macaluso, A. Monteux, and D. Shih, J. High Energy Phys. 08 (2017) 115.

[99] D. Bečirević, S. Fajfer, and N. Košnik, Phys. Rev. D **92,** 014016 (2015).

[100] ATLAS-CONF-2020-049 (2020).

[101] C. Bobeth, M. Gorbahn, T. Hermann, M. Misiak, E. Stamou, and M. Steinhauser, Phys. Rev. Lett. **112,** 101801 (2014).

[102] G. Aad *et al.* (ATLAS Collaboration), Phys. Rev. Lett. **127,** 141801 (2021).

[103] G. Aad *et al.* (ATLAS Collaboration), Phys. Rev. D **90,** 052001 (2014).

[104] D. A. Faroughy, A. Greljo, and J. F. Kamenik, Phys. Lett. B **764,** 126 (2017).

[105] A. Greljo and D. Marzocca, Eur. Phys. J. C **77,** 548 (2017).

[106] Y. Afik, J. Cohen, E. Gozani, E. Kajomovitz, and Y. Rozen, J. High Energy Phys. 08 (2018) 056.

[107] Y. Afik, S. Bar-Shalom, J. Cohen, and Y. Rozen, Phys. Lett. B **807,** 135541 (2020).

[108] A. M. Sirunyan *et al.* (CMS Collaboration), J. High Energy Phys. 07 (2021) 208.

[109] J. Alwall, R. Frederix, S. Frixione, V. Hirschi, F. Maltoni, O. Mattelaer, H. S. Shao, T. Stelzer, P. Torrielli, and M. Zaro, J. High Energy Phys. 07 (2014) 079.

[110] A. Chakraborty and S. Chakraborty, Phys. Rev. D **93,** 075035 (2016).

[111] A. Angelescu, D. Bečirević, D. A. Faroughy, F. Jaffredo, and O. Sumensari, Phys. Rev. D **104,** 055017 (2021).

[112] L. Calibbi, A. Crivellin, and T. Ota, Phys. Rev. Lett. **115,** 181801 (2015).

[113] A. Bhaskar, D. Das, T. Mandal, S. Mitra, and C. Neeraj, Phys. Rev. D **104,** 035016 (2021).

[114] K. Ban, Y. Jho, Y. Kwon, S. C. Park, S. Park, and P.-Y. Tseng, arXiv:2104.06656.

[115] L. Calibbi, A. Crivellin, and T. Li, Phys. Rev. D **98,** 115002 (2018).

[116] R. Barbieri and A. Tesi, Eur. Phys. J. C **78,** 193 (2018).

[117] M. Blanke and A. Crivellin, Phys. Rev. Lett. **121,** 011801 (2018)..

[118] C.-H. Chen, T. Nomura, and H. Okada, Phys. Lett. B **774,** 456 (2017).

[119] A. Crivellin, D. Müller, and T. Ota, J. High Energy Phys. 09 (2017) 040.

[120] I. Bigaran, J. Gargalionis, and R. R. Volkas, J. High Energy Phys. 10 (2019) 106.

[121] A. Crivellin, D. Müller, and F. Saturnino, J. High Energy Phys. 06 (2020) 020.

[122] S. Saad, Phys. Rev. D **102,** 015019 (2020).

[123] K. S. Babu, P. S. B. Dev, S. Jana, and A. Thapa, J. High Energy Phys. 03 (2021) 179.

[124] M. Bauer and M. Neubert, Phys. Rev. Lett. **116,** 141802 (2016).

[125] A. Carvunis, A. Crivellin, D. Guadagnoli, and S. Gangal, Phys. Rev. D **105,** L031701 (2022).

[126] A. Angelescu, D. Becirevic, D. A. Faroughy, and O. Sumensari, J. High Energy Phys. 10 (2018) 183.

[127] J. Grygier et al. (Belle Collaboration), Phys. Rev. D **96,** 091101 (2017); **97,** 099902(A) (2018).

[128] A. J. Buras, J. Girrbach-Noe, C. Niehoff, and D. M. Straub, J. High Energy Phys. 02 (2015) 184.

[129] W. Altmannshofer et al. (Belle-II Collaboration), Prog. Theor. Exp. Phys. **2019,** 123C01 (2019); **2020,** 029201(E) (2020).

[130] L. J. Hall and M. Suzuki, Nucl. Phys. **B231,** 419 (1984).

[131] K. S. Babu and R. N. Mohapatra, Phys. Rev. Lett. **64,** 1705 (1990).

[132] N. Aghanim et al. (Planck Collaboration), Astron. Astrophys. **641,** A6 (2020).

[133] G. Moreau and M. Chemtob, Phys. Rev. D **65,** 024033 (2001).

[134] J. Brod, M. Gorbahn, and E. Stamou, Phys. Rev. D **83,** 034030 (2011).

[135] D. Buttazzo, A. Greljo, G. Isidori, and D. Marzocca, J. High Energy Phys. 11 (2017) 044.

[136] M. Bordone, B-physics in the standard model and beyond, Ph.D. thesis, Zurich University, 2018.

[137] L. Di Luzio, M. Kirk, A. Lenz, and T. Rauh, J. High Energy Phys. 12 (2019) 009.

[138] A. J. Buras, S. Jager, and J. Urban, Nucl. Phys. **B605,** 600 (2001).

[139] A. Bazavov et al. (Fermilab Lattice, MILC Collaborations), Phys. Rev. D **93,** 113016 (2016).

[140] P. A. Boyle, L. Del Debbio, N. Garron, A. Juttner, A. Soni, J. T. Tsang, and O. Witzel (RBC/UKQCD Collaboration), arXiv:1812.08791.

[141] S. Aoki et al. (Flavour Lattice Averaging Group), Eur. Phys. J. C **80,** 113 (2020).

[142] R. Aaij et al. (LHCb Collaboration), Phys. Lett. B **725,** 15 (2013).

[143] M. Misiak et al., Phys. Rev. Lett. **114,** 221801 (2015).